

A New Bayesian Framework with Natural Priors to Constrain the Neutron Star Equation of State

Boyang Sun,¹ Tianqi Zhao,^{2,3} and James M. Lattimer¹

¹*Department of Physics & Astronomy, Stony Brook University, Stony Brook, NY 11794 USA*

²*Institute for Nuclear Theory, University of Washington, Seattle, Washington 98195, USA*

³*N3AS, University of California, Berkeley, Berkeley, California 94720, USA*

(Dated: January 9, 2026)

We propose a new Bayesian framework to infer the neutron star equation of state (EOS) from mass and radius observations and neutron matter theory by defining priors that directly parameterize mass-radius space instead of pressure-energy density space. We use direct and accurate inversion approximations to map mass-radius relations to the underlying EOS. We systematically compare its EOS inferences with those inferred from traditional EOS parameterizations, taking care to quantify the systematic prior uncertainties of both. Our results show that prior uncertainties should be included in all Bayesian approaches. The more natural alternative framework provides broader coverage of the physically allowed mass-radius space, especially small radius configurations, and yields enhanced computational efficiency and substantially reduced dependence on prior choices. Our results demonstrate that direct parameterization in observed space offers a robust and efficient alternative to traditional methods.

Introduction.—The equation of state (EOS) of dense matter at densities in excess of the nuclear saturation density ($n_s \simeq 0.16 \text{ fm}^{-3}$), such as is found in neutron stars [1, 2], is not easily accessible from terrestrial experiments or first-principle theoretical calculations. But since the EOS, specifically the pressure-energy density relation for cold matter, is all that is needed to predict neutron star observables such as masses, radii, moments of inertia, tidal deformabilities and oscillation frequencies, observations can constrain it. Due to the lack of an exact analytical method to invert Tolman-Oppenheimer-Volkoff (TOV) structure equations applicable to neutron stars, Bayesian approaches have been extensively used to infer limits to the equations of state from observations of neutron stars and nuclear experiments and theory [3–6]. In the traditionally-used framework, the model prior probability $\mathcal{P}(\mathcal{M})$ is associated with selected parameterized EOS. Each EOS model, together with each possible set of parameters, generates a particular model $\mathcal{M}(\theta, \mathcal{E})$ in terms of the EOS parameters θ and central energy densities \mathcal{E} . Another input is the prior probability associated with the observed data, usually probability distributions in mass-radius (M - R) space, which we call $\mathcal{P}(\mathcal{D})$. The posterior distribution is then

$$\mathcal{P}(\mathcal{M}(\theta, \mathcal{E})|\mathcal{D}) \propto \mathcal{P}(\mathcal{D}|\mathcal{M}(M, R))\mathcal{P}(\mathcal{M}(\theta, \mathcal{E})),$$

which inevitably involves a mapping $(\theta, \mathcal{E}) \rightarrow (M, R)$ to obtain the likelihood $\mathcal{P}(\mathcal{D}|\mathcal{M}(M, R))$ from the sampling of prior distributions $\mathcal{P}(\mathcal{M}(\theta, \mathcal{E}))$. Moreover, the posterior distributions will somewhat depend on the prior choices. Even when only considering a single EOS parameterization, one also has to consider how its parameters are chosen. For example, should one choose parameters uniformly within their physically allowed bounds, or should their parameters be chosen uniformly in log space? Or should they be chosen so that central values

are emphasized? “Uniformity” is another issue because the corresponding M - R space may not be uniformly covered.

These arbitrary choices will therefore contribute to inherent prior uncertainties that add to observational uncertainties in estimating the underlying EOS. In most analyses to date, this prior uncertainty is largely unquantified, let alone considered, but could be comparable to observational or theoretical uncertainties. Some recent works have, however, studied how the choices of EOS parametrization or astrophysical assumptions could affect the Bayesian inferences [7, 8]. We aim to further clarify prior uncertainties and quantify them.

An alternative approach is to directly parameterize M - R space, which naturally circumvents the issue of EOS parameterizations. In this new framework, both the prior and posterior distributions are in M - R space, which forms a more “natural” prior. After applying constraints from astronomical observations, causality, a lower limit for the neutron star maximum mass (M_{\max}), neutron matter theory and nuclear experiments, it is possible to obtain the posterior distributions of EOS variables, i.e., pressure, energy density, chemical potential and number density, using inversion formulae developed by Sun and Lattimer [9]. The posterior of this alternative method still depends on choices of modeling priors, although these are now defined in M - R space instead of EOS space. Specifically, M - R curves can be chosen arbitrarily throughout the allowed space, or in some regulated fashion such as making the density of radius values uniform at $M = 1.4 M_{\odot}$.

In order to estimate systematic prior uncertainties for both new and traditional frameworks, we compare the posteriors from a series of calculations employing different EOS or M - R space parameterizations, as well as different theoretical neutron matter EOS choices.

Methodology.—The alternative method we propose, which we refer as the Parameterized Mass-Radius (PMR) method, is practical because we employ a highly accurate analytical scheme [9] to invert the TOV equations $[(M, R) \rightarrow (P, \mathcal{E})]$. Specifically, given an entire M - R curve, one determines the masses and radii at 11 fractional maximum mass (M_{\max}) points $f \in [1, 0.95, 0.90, 0.85, 0.8, 0.75, 2/3, 0.6, 0.5, 0.4, 1/3]$. The thermodynamic properties at the center of a star of mass M_f are given by

$$G_f = a_{Gf} \left(\frac{M_{\max}}{M_{\odot}} \right)^{b_{Gf}} \left(\frac{R_g}{10 \text{ km}} \right)^{c_{Gf}} \left(\frac{R_h}{10 \text{ km}} \right)^{d_{Gf}}, \quad (1)$$

where G_f represents the central energy density \mathcal{E} , pressure P , sound speed $c_s/c = \sqrt{dP/d\mathcal{E}}$, chemical potential μ , or baryon number density n of a star with mass $M_f = M/M_{\max}$. a_{Gf} , b_{Gf} , c_{Gf} , and d_{Gf} are constant fitting parameters. R_g and R_h are the radii of stars at fractional maximum masses M_g and M_h , where $g, h \in [f]$; the values of g and h are also parameters of the scheme. Therefore, the scheme, for each thermodynamic quantity, has a 6×11 matrix consisting of 6 constants $(a_{Gf}, b_{Gf}, c_{Gf}, d_{Gf}, g, h)$ for each f . The central conditions for masses intermediate to gridded values at M_f are determined by logarithmic interpolation.

Establishing the M - R boundary.—The first step in the PMR scheme is to establish the physically-realistic boundaries of M - R space, as investigated, for example, in Drischler *et al.* [10]. This step is comparable to traditional approaches used to define the boundaries of the allowed EOS in baryon density–chemical potential space prior to EOS parameterization [11, 12]. For the low-density regime we adopted the SLy4 crustal EOS [13] below a density of 0.04 fm^{-3} , represented as a piecewise polytropic (PP) [14]. Above this density, up to a transition density $n_t = 1.5n_s$, we use the central value together with the $1-\sigma$ uncertainty band from the N³LO χ EFT calculations of neutron star matter [10, 15, 16]. At the density n_t , for the central values of the N³LO EOS, the NS mass is $M_t \simeq 0.45M_{\odot}$, the NS radius is $R_t \simeq 13.0 \text{ km}$, and the pressure is $P_t \simeq 9 \text{ MeV fm}^{-3}$.

To generate the smallest radius for a given mass greater than M_t , a first-order phase transition with constant pressure P_t is assumed, extending up to a critical energy density $\mathcal{E}_c \simeq 0.63 \text{ GeV fm}^{-3}$. Above \mathcal{E}_c , the EOS is taken to be causal with the sound speed $c_s = c$. \mathcal{E}_c is set by the requirement that $M_{\max} = 2.0M_{\odot}$ can be achieved. On the other hand, the largest NS radius for $M > M_t$ is obtained using an EOS with $c = c_s$ for $n \geq n_t$. The maximum mass point along the maximum radius line connects to the corresponding minimum radius point at $2.0M_{\odot}$, closing the allowed region. The resulting bounded region in M - R space is illustrated in Fig. 1 using the central value of the N3LO EOS.

Constructing the M - R mesh.—We proceed to parameterize the bounded M - R space directly by constructing

a discrete mesh with evenly-spaced horizontal grid lines separated by $0.1M_{\odot}$ to specify M , and angled grid lines separated by 0.2 km to specify R , as illustrated in Fig. 1. The grid is anchored to the fixed point (M_t, R_t) . Instead of using vertical fixed radius grid lines, we chose a slope determined by the largest value of dM/dR between intersections of the right-hand boundary of the permitted M - R space with the grid points. This slope consequently depends upon the assumed mass grid spacing. Technically, the maximum slope along the right-hand boundary is infinity, but the discrete grid almost always assures finiteness. However, the smaller the grid mass spacing, the larger the radial grid slope. For the central value of the N³LO EOS, we obtain $dM/dR = 2.2M_{\odot} \text{ km}^{-1}$. Choosing a trapezoidal grid instead of a rectangular grid turns out to not only speed computations of physically possible M - R curves, discussed below, but also prevents those curves from jumping back and forth between adjacent radial grid lines. The latter can occur for a rectangular grid. Masses and radii within the mesh are determined from bilinear interpolation.

Generating M - R curves.—Next, all possible, physically realistic, continuous M - R curves are constructed by successively connecting grid points starting from the fixed point (M_t, R_t) and ending at a point having a mass greater than or equal to the assumed minimum value of M_{\max} , namely $2.0M_{\odot}$. Succeeding segments increase the mass by one unit and can initially either follow the minimum or maximum radius boundaries, or extend to the same or smaller radial grid lines such that the inverse slope dR/dM is non-increasing. After an arbitrary transition point, this condition is replaced by a non-decreasing dR/dM . The curve can instead terminate if the mass is equal to or larger than the minimum assumed M_{\max} . We do not consider the possibility to extend to a new point with the same mass and a smaller radius, as first-order phase transitions are not well fit by our inversion formulae, and extension to a larger radius is disallowed by requirements of causality or thermodynamic stability (as determined below). Segments that would extend to a mesh point outside of the M - R boundary are disallowed. At present, each segment extends only to the next larger mass, but in the future we will allow segments to span more than one mass unit.

Each M - R curve is then accepted or rejected depending on whether or not its inferred P - \mathcal{E} relation determined by Eq. (1) satisfies causality and thermodynamic stability at every density. In this way, M - R space is filled with the surviving M - R curves rather than with the traditional series of M - R curves generated from a parameterized EOS. The probability \mathcal{P} of a given M - R curve $\mathcal{M}_j(M, R)$ under this framework is the posterior probability distribution computed using Bayes’ theorem

$$\mathcal{P}(\mathcal{M}_j(M, R) | \mathcal{D}) \propto \Pi_i \mathcal{P}(\mathcal{D}_i | \mathcal{M}_j(M, R)) \mathcal{P}(\mathcal{M}_j(M, R)),$$

where $i \in 1, 2, 3$ to corresponds to data from the three

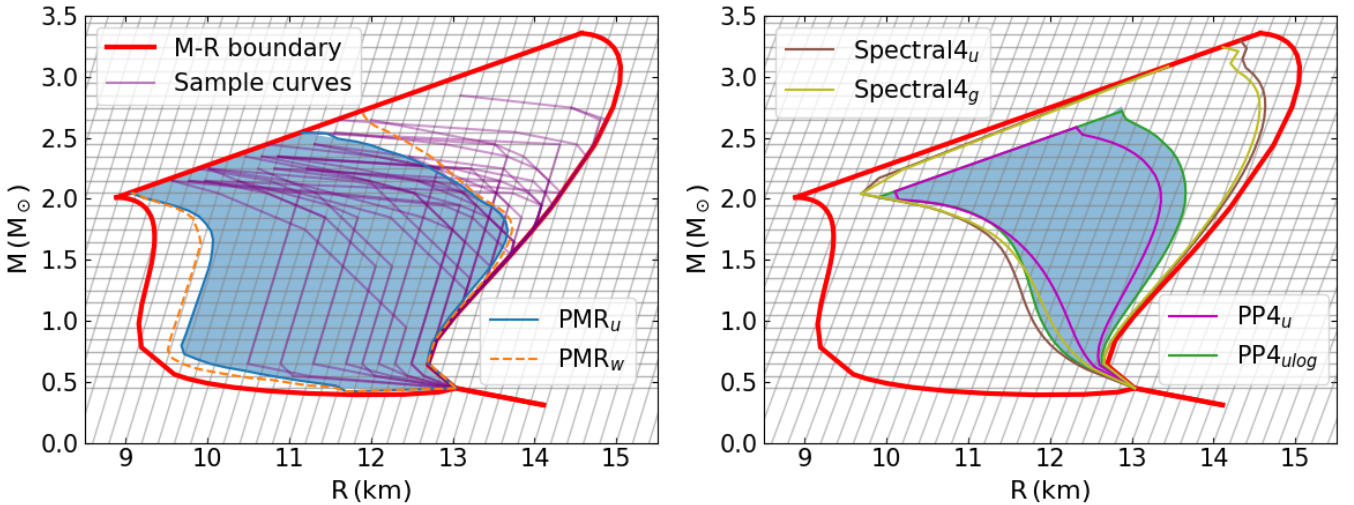


FIG. 1. Left panel: An illustration of the PMR method, showing the adopted M - R mesh (thin lines) as well as the allowed M - R boundary (thick red line). Sample M - R curves are indicated as purple lines. 95% confidence regions for the PMR_u and PMR_w priors are shown as the blue region and enclosed by the dotted dashed orange curve, respectively. Right panel: Together with the allowed M - R bounds and the PMR mesh as a backdrop, the 95% confidence regions for the traditional Bayesian methods using the PP4 and spectral parameterized EOSs are shown. For both, parameters were sampled either uniformly (subscript “u”), log-uniformly (subscript “ ulog ”), or from a Gaussian distribution (subscript “g”).

NICER observations PSR J0740+6620 [17], PSR J0437-4715 [18] and PSR J0030+0451 [19]. Note that all points along the same M - R curve share an identical posterior probability $\mathcal{P} = \mathcal{P}(\mathcal{M}_j(M, R) | \mathcal{D})$. Once the posterior probability distribution of M - R curves is obtained, we derive the corresponding pressure-energy density (P - \mathcal{E}) posterior using Eq. (1).

One distinction between the PMR method and traditional Bayesian approaches lies in the fitting formula uncertainty. Although the fitting errors are typically below 1%, they should be taken into account. Specifically, we assume a Gaussian-like error distribution, so the corrected P - \mathcal{E} probability density for a M - R curve can be expressed as

$$f(\mathcal{E}, P) = \sum_i \frac{\mathcal{P}_i}{2\pi\sigma_{P_i}\sigma_{\mathcal{E}_i}} \exp \left[-\frac{(\mathcal{E} - \mu_{\mathcal{E}_i})^2}{2\sigma_{\mathcal{E}_i}^2} - \frac{(P - \mu_{P_i})^2}{2\sigma_{P_i}^2} \right], \quad (2)$$

where i denotes a fractional M_{\max} point on that curve, $\mu_{\mathcal{E}_i}$ and μ_{P_i} are the central values computed from the analytic inversion formulae, and $\sigma_{\mathcal{E}_i}$ and σ_{P_i} are the given mean uncertainties of those values (as given in Ref. [9]), and \mathcal{P}_i is the posterior probability associated with that point. The total probability density distribution, $f_{\text{tot}}(\mathcal{E}, P)$, is then obtained by summing over all M - R curves sampled in the Bayesian analysis, from which the EOS distribution can be directly derived by integrating over the M - R space. Resulting confidence bands in P - \mathcal{E} space are shown in the left panel of Fig. 2.

Note the initial probabilities of each M - R curve (before introduction of observational data) are equal, but the probabilities of a given grid point (M_i, R_j) , determined

from the number of times M - R curves pass through that point, are not. The initial grid point probabilities effectively form a prior M - R space probability distribution.

Choices of natural priors.—We systematically explore three representative prior distributions to illustrate the impact of prior assumptions on the inferred EOS posteriors in the PMR method.

Prior 1, Uniform sampling in M - R Space: Each M - R curve is granted equal weight. The resulting density distribution of grid points is non-uniform, as more curves populate the central region than the boundaries. This is expected due to the central limit theorem (curves near the boundaries require more extreme physical conditions). The 95% confidence region for this prior, labeled PMR_u , is shown as the blue shaded region in the left panel of Fig. 1. The count at any grid point naturally decreases with increasing distance from the fixed point (M_t, R_t) .

Prior 2, Uniform distribution of $R_{1.4}$ values: To achieve a more radially uniform grid density, we first group M - R curves by their M_{\max} value. We could just treat each group equally and obtain a more uniform radius distribution by weighting curves by the inverse count at a typical NS radius, $R_{1.4}$. However, the curves having large M_{\max} cannot reach small $R_{1.4}$ values. Instead, we correct by additionally weighting them by the number of curves within each M_{\max} group. This produces a more uniform probability distribution of $R_{1.4}$ values for each M_{\max} group, and its 95% confidence region, labeled PMR_w , is enclosed by the magenta dot-dashed curve in the left panel of Fig. 1.

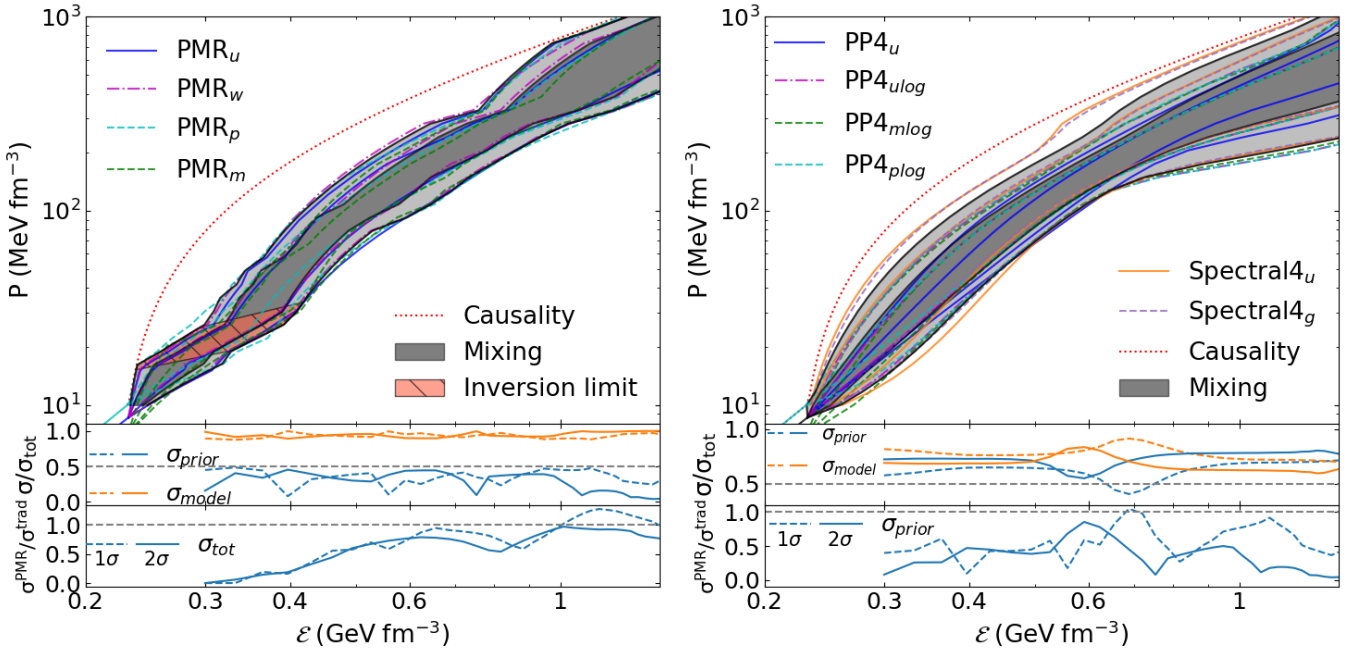


FIG. 2. Comparison of Bayesian results of PMR (left) and traditional methods (right). Left: the upper panel shows the 1- σ and 2- σ boundaries of three priors discussed in *Methodology*. The coral-colored shaded region in the left panel is a region our inversion formula may not reach, corresponding to masses less than $1/3M_{\text{max}}$, below which the boundaries are obtained by linear interpolation. The first lower panel shows the ratios of σ_{prior} and σ_{model} to σ_{tot} for 300–1400 MeV fm $^{-3}$ for 1- σ (dashed lines) and 2- σ (solid lines), respectively. The second lower panel shows the ratio of σ_{tot} of the PMR to the traditional methods. Right: similar to the left panel, but for traditional Bayesian methods, with the second lower panel showing the ratios of σ_{prior} of the two approaches.

Prior 3, Variation of the N³LO boundaries: To straightforwardly assess the impact of systematic uncertainties associated with the N³LO EOS, we vary it between its stated 1- σ upper and lower bounds, while otherwise uniformly sampling EOS curves as in Prior 1. These prior choices are labeled in Fig. 2 as PMR $_p$ and PMR $_m$, respectively, and change the fixed point to which the mesh is anchored slightly. For PMR $_p$, $(M_t, R_t) \simeq (0.52 M_{\odot}, 13.2 \text{ km})$, whereas for PMR $_m$, $(M_t, R_t) \simeq (0.35 M_{\odot}, 13.0 \text{ km})$.

To benchmark our PMR framework, we also undertake traditional Bayesian calculations using two commonly used EOS parameterizations: a four-parameter piecewise-polytropic model (PP4) and a four-parameter spectral expansion (Spectral4). We examine linearly (labeled PP4 $_u$ and Spectral4 $_u$) as well as logarithmically uniform parameter sampling for PP4 (PP4 $_{ulog}$). We also consider a Gaussian sampling for Spectral4 (Spectral4 $_g$) parameters within their allowed ranges. Furthermore, we vary as well the N³LO EOS, using the same notations as for the PMR approach, to ensure a consistent comparison. A minimum M_{max} value of $2.0M_{\odot}$ is again adopted, and causality and thermodynamic stability are enforced in all cases. A detailed description of these parameterizations is provided in Supplemental material.

The right-hand panel of Fig. 1 shows the correspond-

ing 95% confidence regions for traditional Bayesian approaches with various assumed priors. It is apparent that the small radius region is under-represented compared to the PMR method, irrespective of assumed priors in either method. On the other hand, the PMR method seems to under-populate the large radius and high mass regions. It is also clear that the PP4 parameterization is not able to fully represent the region near the upper boundary of the allowed M - R space. Overall, the differences between uniform, log-uniform and Gaussian parameter sampling are seen to be small.

Results.—We highlight two important issues that arise from our analysis. First, we examine the relative importance of prior modeling uncertainties in the PMR and traditional EOS Bayesian methods relative to the observational uncertainties. Second, we examine the relative accuracies of the two approaches when confronted with the same astrophysical data.

To determine the systematic prior uncertainties of each inference scheme, we applied the *model mixing method*, a statistical framework widely used for combining model ensembles in nuclear and astrophysical analyses (e.g., [20, 21]). At each energy density ϵ , the posteriors of each prior for each scheme yields a distribution of possible pressures P . Each prior provides a kernel density estimate (KDE) $\hat{f}_i(P | \epsilon)$. Weighting each prior equally,

the total variance of P at \mathcal{E} is

$$\sigma_{tot}^2(\mathcal{E}) = \int [P(\mathcal{E}) - \bar{P}(\mathcal{E})]^2 \hat{f}_{mix}(P|\mathcal{E}) dP, \quad (3)$$

where \hat{f}_{mix} is the mean of the KDEs for all priors, and \bar{P} is the average pressure of all the prior choices. The total uncertainty can be decomposed into two distinct contributions

$$\sigma_{tot}^2(\mathcal{E}) = \sigma_{model}^2(\mathcal{E}) + \sigma_{prior}^2(\mathcal{E}), \quad (4)$$

where σ_{model} denotes the average intrinsic uncertainty of individual models, while σ_{prior} quantifies how strongly the inferred pressure depends on assumed priors. Results for various assumed priors for the PMR and traditional Bayesian approaches are presented in the left and right panels, respectively, of Fig. 2.

Overall, the posteriors of PMR exhibit behavior broadly similar to those from traditional methods across the full energy-density range. However, the sensitivity to prior assumptions differs significantly. Quantitatively, the fraction of posterior variance attributable to prior choices, quantified by $\sigma_{prior}/\sigma_{tot}$ from Eqs. (3) and (4), remains below 50% in the PMR method, while traditional frameworks show substantially higher sensitivity, with mean values around 70% and typical variations of 50–80%. This indicates that the new natural framework is less affected by prior selection.

Further, as shown in the second lower panel of the left figure in Fig. 2, the 2- σ bounds of the absolute values of σ_{tot} of PMR is generally smaller over the entire energy density range, while the 1- σ bounds are slightly larger for $\mathcal{E} \gtrsim 1 \text{ GeV fm}^{-3}$. We also see that the absolute values of σ_{prior} for PMR are generally smaller for all \mathcal{E} .

Conclusion and outlook.— Our result show that Bayesian inference on the NS EOS are significantly influenced by prior choices which introduce sizable systematic uncertainties, therefore highlighting the importance of assessing multiple prior choices when applying Bayesian methods to NS observations. When this is impractical, a conservative estimate of the prior-induced variance, $\sigma_{prior}^2 \simeq 0.5\sigma_{tot}^2$, may be adopted based on our results for typical traditional frameworks.

The newly developed PMR method offers several advantages: (1) both the natural priors and observational data are defined in the M - R space, making it more direct and intuitive when comparing with observational posteriors; (2) computations are generally much faster because EOS parameterization and repeated TOV solutions are avoided; (3) their prior distributions cover a broader physically allowed M - R region, especially the small radius region as demonstrated in Fig. 1; (4) the posteriors exhibit significantly lower sensitivity to prior assumptions; and (5) it also generally has a smaller total uncertainty when confronted with the same observational data.

The results can be further improved by reducing the uncertainty of the inversion formulae from Ref. [9]. The transformation from the M - R relation to the P - \mathcal{E} relation in Eq. (1) could, for example, be modeled using a neural network [22–26], while the M - R prior is kept unchanged and defined in the same parameter space as the M - R likelihood. This approach can potentially incorporate a wider variety of EOSs with different degrees of freedom and achieve higher fidelity.

More broadly, our findings underscore the need for alternative inference frameworks that offer broader coverage of prior space and reduced dependence on subjective prior assumptions. Such developments will help improve both the reliability and the precision of neutron star EOS constraints from observations. Future work will explore more complex M - R relations, including those with multiple phase transitions, enabled by improved inversion techniques capable of mapping such M - R curves to corresponding EOSs with high accuracy. Recent progress using gradient descent initialized by the current inversion formula following Li *et al.* [27] has yielded encouraging results, suggesting that combining it with machine-learning approaches is a promising next step.

Acknowledgments.— B.S. and J.M.L. acknowledge funding from the US Department of Energy under Grant DE-FG02-87ER40317. T.Z. acknowledges support by the Network for Neutrinos, Nuclear Astrophysics and Symmetries (N3AS) through the National Science Foundation Physics Frontier Center, Grant No. PHY-2020275. We thank Chun Huang, Alan Calder, Douglas Swesty, Sophia Han, Zidu Lin, Shuzhe Shi and Xihai Luo for helpful discussions.

- [1] J. M. Lattimer and M. Prakash, Neutron star structure and the equation of state, *The Astrophysical Journal* **550**, 426 (2001).
- [2] B. Sun, S. Bhattacharyya, and J. M. Lattimer, Compiled properties of nucleonic matter and nuclear and neutron star models from nonrelativistic and relativistic interactions, *Phys. Rev. C* **109**, 055801 (2024).
- [3] L. Brandes, W. Weise, and N. Kaiser, Evidence against a strong first-order phase transition in neutron star cores: Impact of new data, *Phys. Rev. D* **108**, 094014 (2023).
- [4] N. Rutherford, M. Mendes, I. Svensson, A. Schwenk, A. L. Watts, K. Hebeler, J. Keller, C. Prescod-Weinstein, D. Choudhury, G. Raaijmakers, T. Salmi, P. Timmerman, S. Vinciguerra, S. Guillot, and J. M. Lattimer, Constraining the dense matter equation of state with new nicer mass-radius measurements and new chiral effective field theory inputs, *The Astrophysical Journal Letters* **971**, L19 (2024).
- [5] P. J. Kalita, T. Malik, T. Zhao, B. Kumar, and J. M. Lattimer, Observable signatures of quarkyonic phase in neutron stars, *arXiv preprint arXiv:2510.23405* (2025).
- [6] X. Dong, H. Shen, J. Hu, and Y. Zhang, Equation of state for neutron stars with speed of sound constraints

via bayesian inference, *Phys. Rev. D* **112**, 063043 (2025).

[7] J.-J. Li and A. Sedrakian, Bayesian inferences on covariant density functionals from multimessenger astrophysical data: The impacts of likelihood functions of low density matter constraints, *Phys. Rev. C* **112**, 015802 (2025).

[8] A. Kedia, R. O'Shaughnessy, L. Wade, and A. Yelikar, Astrophysical assumptions and equation of state framework have larger impact on equation of state inference than individual neutron star observations (2025), arXiv:2405.17326 [astro-ph.HE].

[9] B. Sun and J. M. Lattimer, Correlations between the neutron star mass-radius relation and the equation of state of dense matter, *The Astrophysical Journal* **984**, 30 (2025).

[10] C. Drischler, S. Han, J. M. Lattimer, M. Prakash, S. Reddy, and T. Zhao, Limiting masses and radii of neutron stars and their implications, *Physical Review C* **103**, 10.1103/physrevc.103.045808 (2021).

[11] D. Zhou, Reexamining constraints on neutron star properties from perturbative qcd, *Physical Review C* **111**, 015810 (2025).

[12] T. Gorda, O. Komoltsev, A. Kurkela, and E. Sunde, Constrained brownian-bridge prior for neutron-star equation-of-state inference, arXiv preprint arXiv:2512.18044 (2025).

[13] E. Chabanat, P. Bonche, P. Haensel, J. Meyer, and R. Schaeffer, A skyrme parametrization from subnuclear to neutron star densities part ii. nuclei far from stabilities, *Nucl. Phys. A* **635**, 231 (1998).

[14] T. Zhao and J. M. Lattimer, Universal relations for neutron star *f*-mode and *g*-mode oscillations, *Phys. Rev. D* **106**, 123002 (2022).

[15] C. Drischler, J. Melendez, R. Furnstahl, and D. Phillips, Quantifying uncertainties and correlations in the nuclear-matter equation of state, *Physical Review C* **102**, 054315 (2020).

[16] C. Drischler, K. Hebeler, and A. Schwenk, Chiral interactions up to next-to-next-to-next-to-leading order and nuclear saturation, *Physical Review Letters* **122**, 042501 (2019).

[17] T. Salmi, D. Choudhury, Y. Kini, T. E. Riley, S. Vinciguerra, A. L. Watts, M. T. Wolff, Z. Arzoumanian, S. Bogdanov, D. Chakrabarty, K. Gendreau, S. Guillot, W. C. G. Ho, D. Huppenkothen, R. M. Ludlam, S. M. Morsink, and P. S. Ray, The radius of the high-mass pulsar psr j0740+6620 with 3.6 yr of nicer data, *The Astrophysical Journal* **974**, 294 (2024).

[18] D. Choudhury, T. Salmi, S. Vinciguerra, T. E. Riley, Y. Kini, A. L. Watts, B. Dorsman, S. Bogdanov, S. Guillot, P. S. Ray, D. J. Reardon, R. A. Remillard, A. V. Bilous, D. Huppenkothen, J. M. Lattimer, N. Rutherford, Z. Arzoumanian, K. C. Gendreau, S. M. Morsink, and W. C. G. Ho, A nicer view of the nearest and brightest millisecond pulsar: Psr j0437–4715, *The Astrophysical Journal Letters* **971**, L20 (2024).

[19] T. E. Riley, A. L. Watts, S. Bogdanov, P. S. Ray, R. M. Ludlam, S. Guillot, Z. Arzoumanian, C. L. Baker, A. V. Bilous, D. Chakrabarty, K. C. Gendreau, A. K. Harding, W. C. G. Ho, J. M. Lattimer, S. M. Morsink, and T. E. Strohmayer, A nicer view of psr j0030+0451: Millisecond pulsar parameter estimation, *The Astrophysical Journal Letters* **887**, L21 (2019).

[20] A. C. Sempowski, C. Drischler, R. J. Furnstahl, J. A. Melendez, and D. R. Phillips, From chiral effective field theory to perturbative qcd: A bayesian model mixing approach to symmetric nuclear matter, *Phys. Rev. C* **111**, 035804 (2025).

[21] P. Landry and R. Essick, Nonparametric inference of the neutron star equation of state from gravitational wave observations, *Phys. Rev. D* **99**, 084049 (2019).

[22] Y. Fujimoto, K. Fukushima, and K. Murase, Mapping neutron star data to the equation of state using the deep neural network, *Physical Review D* **101**, 054016 (2020).

[23] F. Morawski and M. Bejger, Neural network reconstruction of the dense matter equation of state derived from the parameters of neutron stars, *Astronomy & Astrophysics* **642**, A78 (2020).

[24] S. Soma, L. Wang, S. Shi, H. Stöcker, and K. Zhou, Reconstructing the neutron star equation of state from observational data via automatic differentiation, *Physical Review D* **107**, 083028 (2023).

[25] N. Patra, T. Malik, H. Pais, K. Zhou, B. Agrawal, and C. Providênci, Inferring the equation of state from neutron star observables via machine learning, *Physics Letters B* **865**, 139470 (2025).

[26] W. Zhou, H. Shen, J. Hu, and Y. Zhang, First-order phase transition in a neutron star from a deep neural network, *Phys. Rev. D* **110**, 043017 (2024).

[27] R. Li, S. Han, Z. Lin, L. Wang, K. Zhou, and S. Shi, Toward constraining qcd phase transitions in neutron star interiors: Bayesian inference with a tolman-oppenheimer-volkof linear response analysis, *Phys. Rev. D* **111**, 074026 (2025).

[28] J. S. Read, B. D. Lackey, B. J. Owen, and J. L. Friedman, Constraints on a phenomenologically parametrized neutron-star equation of state, *Physical Review D* **79**, 124032 (2009).

[29] T. Zhao and J. M. Lattimer, Tidal deformabilities and neutron star mergers, *Physical Review D* **98**, 063020 (2018).

[30] L. Lindblom, Spectral representations of neutron-star equations of state, *Physical Review D* **82**, 103011 (2010).

[31] B. Abbott, R. Abbott, T. Abbott, F. Acernese, K. Ackley, C. Adams, T. Adams, P. Addesso, R. Adhikari, V. Adya, *et al.*, Gw170817: Measurements of neutron star radii and equation of state, *Physical review letters* **121**, 161101 (2018).

[32] M. F. Carney, L. E. Wade, and B. S. Irwin, Comparing two models for measuring the neutron star equation of state from gravitational-wave signals, *Physical Review D* **98**, 063004 (2018).

[33] M. C. Miller, C. Chirenti, and F. K. Lamb, Constraining the equation of state of high-density cold matter using nuclear and astronomical measurements, *The Astrophysical Journal* **888**, 12 (2019).

Supplemental Material

A. Piecewise Polytropic (PP) Representation

Following the framework proposed by Read *et al.* [28], high-density, cold nuclear equations of state (EOSs) can be well approximated by a sequence of piecewise-polytropic segments. Each segment is described by the polytropic equation of state $P = K_i n^{\gamma_i}$ for the region $n_{i-1} < n < n_i$, where P is the pressure, n is the baryon number density, and the constants K_i and adiabatic indices refer to the i th segment. Matching conditions at the core-crust transition, together with the continuity of P and the energy density \mathcal{E} at the boundaries, determine K_i , leaving 2 free parameters for each segments—namely, $\{n_i, \gamma_i\}$, or, equivalently, $\{n_i, P_i\}$. Unlike earlier implementations in which the transition densities n_i were fixed [29], we treat the segment boundaries n_i as additional free parameters. In this work, we adopt a modified four-parameter PP4 representation to increase flexibility at high densities, with $i = 1, 2, 3, 4$. Within segment i , the energy density is given by

$$\mathcal{E} = \mathcal{E}_{i-1} \frac{n}{n_{i-1}} + \frac{P - P_{i-1}(n/n_{i-1})}{\gamma_i - 1}, \quad n_{i-1} \leq n \leq n_i, \quad (S1)$$

which follows directly from the standard thermodynamic relation between pressure and energy density for a polytropic EOS. Consistent with PMR method, we choose the transition density $n_0 = 1.5n_s$, rather than matching directly to a crust EOS. The corresponding energy density \mathcal{E}_0 and pressure P_0 are determined from N³LO χ EFT calculations [10]. In the interval $n_0 < n < n_{\max} = 12n_s$, we select four intermediate densities and sort them as $n_0 < n_1 < n_2 < n_3 < n_4 < n_{\max}$. The associated pressures are labeled such that $P_0 < P_1 < P_2 < P_3 < P_4 < P_{\max}$. For the linear prior, $P_{1,2,3,4}$ are sampled uniformly between P_0 and P_{\max} . For the logarithmic prior, $\ln P_{1,2,3,4}$ are sampled uniformly between $\ln P_0$ and $\ln P_{\max}$, which places more weight on the low-pressure end. In both cases, EOS parameter sets that violate causality are excluded.

Bayesian analysis based on PP4 is subject to prior assumptions associated with the finite number of segments, taken to be four in this work, as well as the choice of the energy density and pressure at the lower baryon number density boundary n_0 . The sampling of the transition densities n_i and pressures P_i is not unique and should therefore also be regarded as part of the prior specification. Additional physical constraints, such as causality and thermodynamic stability, are universal requirements for any EOS. However, their impact within the PP4 framework is implementation dependent. For example, thermodynamic stability is enforced by requiring an ordered sequence of pressures, $P_1 < P_2 < P_3 < P_4$, rather than by explicitly rejecting configurations with $P_i > P_j$ for $i < j$. Similarly, violations of causality are more likely to occur at the high density end of each segment, since the corresponding adiabatic indices γ_i are typically larger than 1.

B. Spectral Representation

An alternative and complementary approach is the spectral representation developed by Lindblom [30], which provides an efficient parametrization of smooth, realistic EOSs with relatively few parameters. The method expands the logarithm of the adiabatic index Γ as a Taylor series in the logarithm of pressure:

$$\ln \Gamma(x) = \sum_{i=0}^i \gamma_i x^i, \quad x = \ln \frac{P}{P_0}, \quad (S2)$$

where P_0 is the pressure at a matching density n_0 , consistent with the PP representation. The adiabatic index Γ is related to the thermodynamic derivatives of pressure and energy density via

$$\Gamma(x) = \frac{d(\ln P)}{d(\ln n)} = \frac{\mathcal{E} + P}{P} \frac{dP}{d\mathcal{E}}. \quad (S3)$$

Integrating this relation yields the energy density and baryon number density as

$$\mathcal{E} = \frac{n}{n_0} \left[\mathcal{E}_0 + P_0 \int_0^x \frac{n_0 e^{x'}}{n' \Gamma(x')} dx' \right], \quad \ln \frac{n}{n_0} = \int_0^x \frac{dx'}{\Gamma(x')}. \quad (S4)$$

In the Spectral4 parameterization adopted here, $\ln \Gamma(x)$ is expanded up to third order, including four parameters $\gamma_0, \gamma_1, \gamma_2, \gamma_3$. Numerical evaluation is performed using quadratic integration for number density and double-quadratic integration for energy density in Eq. (S4). To improve computational efficiency, interpolation is employed after the

initial tabulation of the EOS. Boundary matching at the core–crust interface ensures thermodynamic consistency. The original proposed uniform prior ranges for the spectral parameters are $\gamma_0 \in [0.2, 2]$, $\gamma_1 \in [-1.6, 1.7]$, $\gamma_2 \in [-0.6, 0.6]$, $\gamma_3 \in [-0.02, 0.02]$ [31–33], based on $P_0 \approx 5.4 \times 10^{32}$ corresponds to $n_0 = 0.5n_s$. In this work, we choose the transition density $n_0 = 1.5n_s$ to be consistent with PMR and PP representations. Therefore, we modify the prior range to $\gamma_0 \in [0, 3]$, $\gamma_1 \in [-3, 3]$, $\gamma_2 \in [-1, 1]$, $\gamma_3 \in [-0.2, 0.2]$, which cover the vast majority of the faithful EOSs. We also test the Gaussian prior on these parameter which follows $\gamma_0 \in \mathcal{N}(1.5, 0.75^2)$, $\gamma_1 \in \mathcal{N}(0, 1.5^2)$, $\gamma_2 \in \mathcal{N}(0, 0.5^2)$, $\gamma_3 \in \mathcal{N}(0, 0.1^2)$. In both cases, EOS parameter sets that violate causality and stability are excluded.

Bayesian analysis based on the Spectral4 is likewise subject to several prior assumptions. These include the choice of truncation order in the expansion of $\ln \Gamma(x)$, which is fixed to third order in this work, as well as the selection of the matching density n_0 and the corresponding pressure P_0 and energy density \mathcal{E}_0 . The adopted prior ranges or distributions for the spectral coefficients $\{\gamma_0, \gamma_1, \gamma_2, \gamma_3\}$ constitute an additional and important source of prior dependence. The intrinsic smoothness of the spectral representation further suppresses sharp transition in the EOS, e.g. due to strong phase transitions. In addition, thermodynamic stability and causality must be verified explicitly over the entire density range, rather than being enforced through parameter choice and ordering as in the PP4 representation.